In situ control of the helical and skyrmion phases in Cu_2OSeO_3 using high-pressure helium gas up to 5 kbar

M. Crisanti,[1,2,*] N. Reynolds,[3,4] I. Živković,[4] A. Magrez,[5] H. M. Rønnow,[4] R. Cubitt,[1] and J. S. White[3,†]

[1]*Large Scale Structures Group, Institut Laue-Langevin, 71 avenue des Martyrs, CS 20156, 38042 Grenoble Cedex 9, France*

[2]*Department of Physics, University of Warwick, Coventry CV4 7AL, United Kingdom*

[3]*Laboratory for Neutron Scattering and Imaging, Paul Scherrer Institut, CH-5232 Villigen PSI, Switzerland*

[4]*Laboratory for Quantum Magnetism, Institute of Physics, École Polytechnique Fédérale de Lausanne, CH-1015 Lausanne, Switzerland*

[5]*Crystal Growth Facility, Institute of Physics, École Polytechnique Fédérale de Lausanne, CH-1015 Lausanne, Switzerland*

(Received 7 April 2020; revised manuscript received 13 May 2020; accepted 18 May 2020; published 22 June 2020)

We report a small-angle neutron scattering study of the helical and skyrmion lattice order in single-crystal Cu_2OSeO_3 under quasihydrostatic helium gas pressures up to 5 kbar. By using helium gas as the pressure-transmitting medium (PTM) we ensure pressure application with improved hydrostaticity at cryogenic temperatures compared with previous reports where liquid PTMs were used. For 5-kbar He gas pressure we observe modest changes of the ambient pressure phase diagram; the critical temperature T_c changes by $+2.8(2)\%$, while in the low-T limit the helical propagation vector $|q|$ changes by $-0.5(2)\%$, the lower critical field H_{c1} changes by $+2.5(1.0)\%$, and the upper critical field H_{c2} remains unchanged within uncertainty. The skyrmion phase also changes little under pressure; its largest T extent varies from $T_c - 2.5(5)$ K at ambient pressure to $T_c - 3.0(5)$ K at 5 kbar, and its location in the phase diagram follows the pressure-driven shift of T_c. The weak pressure dependences of the critical magnetic fields and skyrmion phase contrast strongly with much stronger pressure-driven changes reported from previous quasihydrostatic pressure studies. Taking into account the present results and those of other uniaxial pressure data, we suggest that the results of previous quasihydrostatic pressure studies were influenced by inadvertent directional stress pressure components. Overall, our study represents a high-pressure study of the chiral magnetism in Cu_2OSeO_3 under the most hydrostatic high-pressure conditions to date and serves also as a salient reminder of the sensitivity of chiral magnets to deviations from hydrostaticity in quasihydrostatic high-pressure studies.

DOI: 10.1103/PhysRevB.101.214435

I. INTRODUCTION

Skyrmions are topologically protected vortexlike quasiparticles that form a hexagonal lattice in a few chiral cubic magnets under well-defined conditions of temperature T and applied magnetic field $\mu_0 H$ [1–5]. First observed in 2009 from small-angle neutron scattering (SANS) studies of the $B20$ chiral magnet MnSi (space group $P2_13$) [1], skyrmion lattices were observed in other $P2_13$ magnets such as FeGe [4], $Fe_{1-x}Co_xSi$ [3], and Cu_2OSeO_3 [2] and, furthermore, in Co-Zn-Mn alloys which crystallize in a different chiral cubic space group, $P4_132/P4_332$ [6–8]. Common among these chiral cubic magnets is that their equilibrium skyrmion phases are stable over a small parameter space, typically just a few Kelvin wide directly below the magnetic ordering temperature T_c, and in a finite $\mu_0 H$. Recent research efforts into these systems have been focused on a deeper understanding of the stability of the small skyrmion phases close to T_c. Finding ways to enhance the skyrmion phase stability over a broader parameter space could improve the perspective for skyrmion-based applications.

Beyond the skyrmion phase close to T_c, the $\mu_0 H$-T phase diagrams of chiral cubic magnets display a generic structure that is understood in terms of a common hierarchy of magnetic energy scales. The strongest energy scale is an isotropic exchange interaction J that favors a collinear, usually ferromagnetic, arrangement of spins. The second-strongest energy scale is due to the Dzyaloshinskii-Moriya interaction D which exists due to the chiral symmetry of the crystal. The competition between J and D leads to an incommensurate chiral helix ground state that typically modulates over a long period of tens of unit cells. The weakest energy scale is the magnetic anisotropy, which determines the crystallographic alignment of the helical propagation vector q. Due to the long periodicity of the chiral magnetism, the Bak-Jensen [9–12] free-energy expansion for a slowly varying spin density can capture qualitative aspects of the phase diagram and provide simple relations such as $|q| \propto D/J$ that can be compared with experiment. On the other hand, skyrmion phase stability just

*M.Crisanti@warwick.ac.uk

†jonathan.white@psi.ch

below T_c cannot be explained in terms of a standard mean-field theory but, instead, emerges upon inclusion of the effect of thermal fluctuations around the mean-field solution [1,13,14].

Various methods exist for increasing the parameter space over which skyrmions can exist in chiral magnets. One approach is to reduce the sample dimension and make a thin plate, since this leads generally to a destabilization of the conical phase in favor of the skyrmion phase [15]. However, the general structure of the bulk phase diagram is then lost and becomes sample specific and sensitive to the details of the sample preparation. Other approaches for generating extended skyrmion regimes include supercooling through the small skyrmion pocket to create long-lived low-T metastable skyrmion states [3,7,16–22] and using targeted chemical substitution [23,24]. In the latter case, inevitable sample disorder makes theoretical treatment challenging, and, in general, such studies do not necessarily provide the desired insights into skyrmion stability mechanisms.

Applied pressure P, either quasihydrostatic or directional, is, in principle, a clean tuning parameter for the helimagnetic and skyrmion phase diagram of chiral magnets. To date, various high-pressure studies have been performed on the $B20$ compounds [25–37] and Cu_2OSeO_3 [13,31,38–41]. Here we explore the effect of quasihydrostatic pressure on the phase diagram of the latter, the archetypal insulator skyrmion host Cu_2OSeO_3, aiming to clarify a puzzle posed by previous high-pressure work. Previous high-pressure bulk measurements commonly suggest that the application of quasihydrostatic pressure leads to a monotonic increase of T_c [13,31,38,39]. In addition, data from an ac susceptibility study further imply a concomitant, remarkable pressure-driven increase in size of the skyrmion pocket [13]. In that study, the largest T extent of the skyrmion pocket is reported to increase from $T_c - 3$ K at ambient pressure to $T_c - 10$ K at 6 kbar to $T_c - 26$ K at 23 kbar. On the other hand, a separate neutron scattering study of Cu_2OSeO_3 under compressive uniaxial stress revealed skyrmion phase stability could also be enhanced significantly for σ up to 1.01 kbar with no increase in T_c [41]. Since this latter study implies expansion of the skyrmion pocket is achievable with modest uniaxial compressive stress in the kilobar range, it remains unclear if the large expansion of the skyrmion pocket reported in Ref. [13] is a genuine effect of quasihydrostatic pressure or if, instead, it is driven by an inadvertent directional pressure component.

To help clarify this issue, we report new SANS measurements of the microscopic magnetism in single-crystal Cu_2OSeO_3 under quasihydrostatic pressure. To aim for improved hydrostatic pressure conditions compared with previous quasihydrostatic pressure studies, we choose a pressure-transmitting medium (PTM) of He gas. As described by Klotz [42,43], for high-pressure neutron studies, the performance of compressed gases such as He, Ne, and N_2 as pressure-transmitting media at cryogenic T's is always superior compared with commonly used liquid media such as mixtures of deuterated methanol-ethanol and Fluorinert. Most pressure-transmitting media, which are either gas or liquid at room T, inevitably freeze under compression when cooling to cryogenic T. In their low-T solid phases, improved pressure hydrostaticity is achieved with compressed gases due to their lower shear strengths. The compromise in choosing a compressed-gas PTM for improved pressure hydrostaticity is that the maximum pressure that can be achieved is reduced compared to when using a compressed-liquid PTM.

In the present work, we applied high He gas pressure up to 5 kbar to single-crystal Cu_2OSeO_3 and performed low-T SANS measurements. As our main result, we observe only modest pressure-driven changes in both the fundamental aspects of the magnetism and the absolute extent of the skyrmion pocket under pressure. The weak observed quasihydrostatic pressure dependence of the size of the skyrmion pocket contrasts with the results from previous bulk measurements done using a liquid PTM [13,39]. This implies an unanticipated role played by directional stresses in these earlier studies. Here, by avoiding a liquid PTM entirely, we demonstrate an improved methodology for high quasihydrostatic pressure studies of the nanoscale magnetism in chiral magnets. Furthermore, we emphasize the indispensable role of neutron scattering as a microscopic probe of magnetism in the pressurized samples.

II. EXPERIMENT

For the SANS experiments, a 91-mg Cu_2OSeO_3 single crystal ($T_c = 57.9$ K) grown by chemical vapor transport was prealigned and mounted onto an Al pillar inside a 5-kbar Ti-Zr gas pressure cell. The gas pressure cell was installed inside an Orange cryostat, with an external electromagnet providing the applied magnetic field to the sample. We chose an experimental geometry with a horizontal plane defined by orthogonal $[0\bar{1}1]$-[100] axes, with the [110] axis being vertical. The direction of the horizontal $\mu_0 H$ was always kept fixed with respect to the crystal so that $\mu_0 H \parallel [0\bar{1}1]$ [Figs. 1(a) and 1(b)].

SANS measurements were performed using the D33 beamline at the Institut Laue-Langevin (ILL), France, in the two experimental geometries shown in Fig. 1, either $\mu_0 H \perp \mathbf{k}_i$ [Fig. 1(a)], where $\mathbf{k}_i$ is the incident neutron wave vector, or $\mu_0 H \parallel \mathbf{k}_i$ [Fig. 1(b)]. Both geometries are optimized for studying the magnetic scattering intensity in the plane perpendicular to $\mathbf{k}_i$. Thus, in the first geometry we study scattering in the (100) plane, and on zero-field cooling (ZFC), Fig. 1(c) shows that two helical domains described by $\mathbf{q}_1 \parallel (001)$ and $\mathbf{q}_2 \parallel (010)$ can be observed simultaneously (note that both $\pm\mathbf{q}_i$ give a Bragg spot). The alignment of the helical propagation vectors with {100} directions is consistent with other SANS studies of Cu_2OSeO_3 [41,44–48]. In the second geometry, we study the $(0\bar{1}1)$ plane and can observe the third helical domain with $\mathbf{q}_3 \parallel (100)$ [Fig. 1(d)]. The skyrmion phase is best studied in the geometry with $\mu_0 H \parallel \mathbf{k}_i$ since the skyrmions form a skyrmion lattice (SkL) that can be observed as a corresponding sixfold pattern of diffraction peaks all with propagation vectors $\mathbf{q} \perp \mu_0 H$. In contrast, the conical phase with $\mathbf{q}_c \parallel \mu_0 H$ has to be studied in the $\mu_0 H \perp \mathbf{k}_i$ geometry.

D33 was configured with a collimation length of 12.8 m before the sample and a neutron wavelength $\lambda = 6$ Å with a full-width-at-half-maximum spread of $\Delta\lambda/\lambda = 10\%$. The scattered neutrons were detected by a two-dimensional multidetector placed 12.8 m behind the sample. In both experimental geometries, we performed rocking curve measurements of the scattered intensity. In $\mu_0 H = 0$, rocking scan

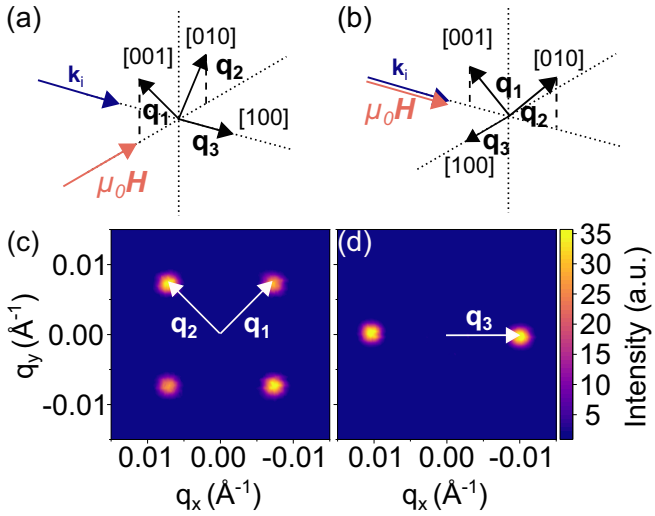

FIG. 1. Illustration of the experimental geometries for the D33 SANS measurements. (a) and (b) show the relative orientations of the crystal cubic axes with respect to the directions of both the incoming neutron wave vector $\mathbf{k}_i$ and the applied magnetic field $\mu_0 H \parallel [0\bar{1}1]$. (a) shows the $\mu_0 H \perp \mathbf{k}_i$ geometry, and (b) shows the $\mu_0 H \parallel \mathbf{k}_i$ geometry. Below T_c and for $\mu_0 H = 0$, the sample is expected to display three helical domains with propagation vectors aligned with the cubic axes [41,44–48]. Typical SANS data shown in (c) are obtained in the first geometry, where two helical domains described by $\mathbf{q}_1 \parallel (001)$ and $\mathbf{q}_2 \parallel (010)$ can be observed. The data shown in (d) were obtained in the second geometry, and the third helical domain with $\mathbf{q}_3 \parallel (100)$ is observed. The SANS data were collected at 30 K and $\mu_0 H = 0$, with $\mathbf{k}_i$ out of the page.

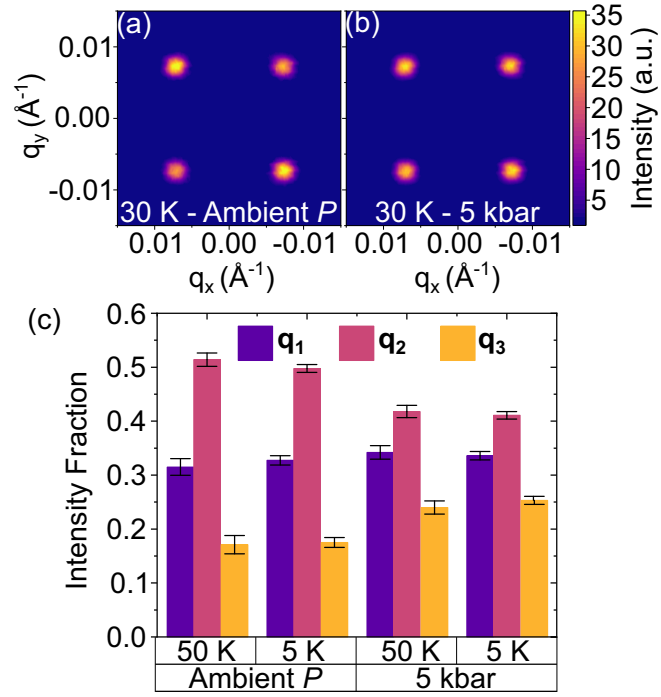

FIG. 2. SANS data from helical order in the (100) plane in $\mu_0 H = 0$. (a) and (b) show SANS patterns each recorded at 30 K at (a) ambient pressure and (b) $P = 5$ kbar. (c) shows a histogram of the relative fraction of each helical domain in the sample at 50 and 5 K and at ambient pressure (left side) and $P = 5$ kbar (right side). In the ideal case, each domain is expected to populate $1/3$ of the sample upon ZFC below T_c.

measurements were done by rotating the gas pressure cell independently of the electromagnet and through the full range of angles that moved the magnetic diffraction spots through the Bragg condition at the detector. From such data the full angle-dependent intensity of the diffraction spots was measured, and the proper integrated intensity was determined. In finite $\mu_0 H$, to keep the magnetic field direction fixed with respect to the sample, the rocking scans were done by rotating the pressure-cell-cryostat-electromagnet assembly together. In this instance, due to the limited opening angle of the electromagnet access windows, the angular range of the scans was restricted to $\pm 3.5^\circ$. Since the restricted range is significantly less than the typical $\sim 15^\circ$ full width at half maximum of the helical peaks in $\mu_0 H = 0$, it was not possible to determine integrated intensities in finite magnetic field. Instead, we estimate the scattered intensity for a spot by summing the observed intensity over the scanned range, leading to a quantity referred to as the SANS intensity.

For measurements done in either zero or finite $\mu_0 H$, detector data were collected at each rocking angle with a typical exposure time of 30 s. To produce the SANS patterns presented in this study, the data obtained at all rocking angles are summed together. All SANS data were collected after zero-field cooling to a target T and after a subsequent application of $\mu_0 H$. Further data were collected in the paramagnetic state at 70 K and used for background subtraction of data taken below T_c. The SANS data reduction and analysis were performed using the GRASP software [49] developed at the ILL.

SANS measurements were performed at either ambient P or an applied pressure of 5 kbar. Unless otherwise stated, the pressure was either applied or released in the paramagnetic state at 70 K. At this T, the He PTM solidifies under a pressure of 12.2 kbar [50]. Therefore, all P changes done at 70 K were done in the liquid phase of the He PTM. Most of the SANS measurements were also performed with PTM in the gas or liquid phase, either over the whole T range at ambient P or above 39.6 K at 5 kbar. Below 39.6 K at 5-kbar pressure, the He PTM does solidify, although as is seen in what follows, no sign of the effect of He solidification is detectable in the SANS data from the sample.

III. RESULTS

A. Helical domain populations and hydrostaticity of the applied pressure

Figure 2 shows pressure- and T-dependent SANS data obtained from the helical phase in $\mu_0 H = 0$. Figure 2(a) shows again the SANS pattern at 30 K and ambient pressure from the (100) plane with the $\mathbf{q}_1$ and $\mathbf{q}_2$ propagation vectors aligned with the $\langle 100 \rangle$ axes and having a magnitude close to 0.01 Å^{-1} [44–48]. While the absolute magnitudes $|q_1| = |q_2|$ within uncertainty, we see by inspection that the integrated intensity of the diffraction spots $I(\mathbf{q}_2)$ are larger than $I(\mathbf{q}_1)$. These data indicate an intrinsic imbalance in helical domain populations exists in the crystal at ambient pressure.

To quantify the domain population imbalance, the left part of Fig. 2(c) shows the fractional population of all three helical domains in the sample at ambient pressure and both 50 and 5 K determined from integrated intensity measurements. In contrast to an ideal population fraction for each domain of 1/3, we find the $\mathbf{q}_2$ domain occupies half of the sample, mainly at the expense of the $\mathbf{q}_3$ domain. The precise origin of the unequal domain population at ambient pressure is challenging to pin down, and it has also been observed previously in other Cu_2OSeO_3 crystals at ambient pressure [41]. The explanation must be due to the presence of directional stresses, which can either be intrinsic to the crystal or have an extrinsic origin in the experiment. In the study by Nakajima *et al.* on uniaxial pressure applied to Cu_2OSeO_3, it was found that a uniaxial stress σ of 0.1 kbar $\perp \mathbf{q}_i$ can lead to a fivefold enhancement of the $\mathbf{q}_i$ domain population, with no change in $|q_i|$ to a level of $\sim$0.1%. In the present study, which displays less overall disparity between the ambient pressure domain fractions than found in Ref. [41], we find all $|q_i|$, $i = 1$–3, to be equal within the experimental accuracy of 0.1%. From this consideration, we thus consider 0.1 kbar to be an upper-limit estimate for undesired directional stresses in our experiment.

Turning to measurements of the helical order obtained under 5-kbar He gas pressure, the SANS pattern in Fig. 2(b) indicates that at 30 K the difference between $I(\mathbf{q}_1)$ and $I(\mathbf{q}_2)$ in fact reduces under pressure compared with ambient pressure. This deduction is augmented by the data shown in the right part of Fig. 2(c), indicating that applied pressure leads to a more balanced domain population compared with that at ambient pressure. The change in domain populations under pressure shows that the applied gas pressure is not perfectly hydrostatic since it modifies the distribution of residual stresses. We note, nonetheless, that the magnitudes of the helical propagation vectors $|q_i|$, $i = 1$–3, remain equivalent within uncertainty and aligned with the $\langle 100 \rangle$ axes, indicating little effect of the residual strains in the sample on the magnetic textures *within* the domains. In addition, the data shown on the right of Fig. 2(c) reveal there is no consequence for the observed helical domain fractions due to the freezing of the He PTM on cooling below 39.6 K. Taken together, we therefore conclude that, besides a modification of the distribution of directional stresses, the 5-kbar applied pressure is, indeed, predominantly hydrostatic.

B. Pressure dependence of helical order and critical magnetic fields at low temperature

Figure 3(a) shows a T-cooling scan for the average of the integrated intensities $I(\mathbf{q}_1)$ and $I(\mathbf{q}_2)$ in the plane. Note that the averaged intensity is lower at 5 kbar than at ambient pressure. This is due to the reduction of $I(\mathbf{q}_2)$ and the concomitant increase of $I(\mathbf{q}_3)$ under pressure [Fig. 2(c)], with the latter not measured in the scan. As shown in detail in the bottom left inset in Fig. 3(a), the value for T_c increases under pressure, increasing from $T_c = 57.9(1)$ K at ambient pressure to $T_c = 59.5(1)$ K at 5 kbar. This leads to a pressure-driven increase of T_c, $\partial T_c/\partial P = +0.32(1)$ K/kbar, in broad agreement with the linear T_c-P relationship determined from previous bulk measurements [13,31,38]. In the top right inset in Fig. 3(a), we show the averaged

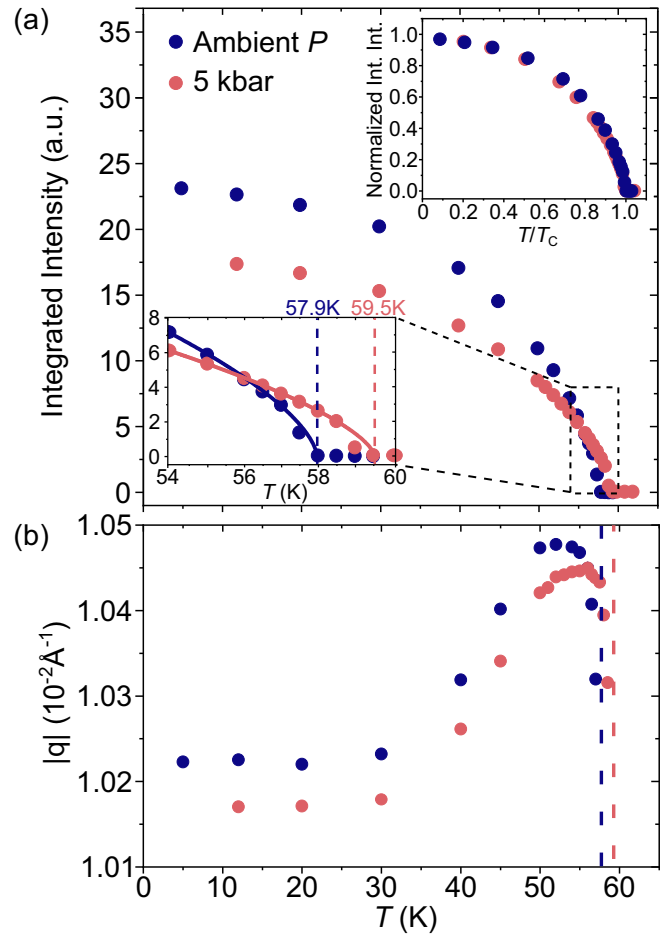

FIG. 3. (a) The pressure and T dependence of the SANS integrated intensity from the helical phase. Each data point is the average $I(\mathbf{q}_1)$ and $I(\mathbf{q}_2)$ in the (100) plane. The lower left inset shows a zoom of the high-T range, where the data are fit with a power law to determine T_c. The upper right inset shows a graph of the SANS integrated intensity normalized by the estimated zero-T value versus T/T_c. (b) The pressure and T dependence of the helical modulation $|q|$ in $\mu_0 H = 0$. The data obtained at 5 kbar in both panels (and their underlying SANS images, data not shown) reveal no obvious effect due to the solidification of the He PTM below 39.6 K.

SANS integrated intensity normalized to its estimated zero-T value versus the normalized temperature T/T_c. From this plot we observe that the intrinsic form of the T dependence of the integrated intensity displays only a weak dependence on pressure up to 5 kbar.

Figure 3(b) shows the pressure and T dependence of the magnitude of the helical propagation vector $|q|$, with the value determined as the average of $|q_1|$ and $|q_2|$. At each pressure, $|q|$ initially falls with decreasing T and eventually plateaus as the renormalization effect due to thermal fluctuations becomes suppressed [1,14]. Under $P = 5$ kbar, the helical $|q|$ is suppressed by $\sim$0.5% compared with its value at ambient pressure over the T range below 50 K. In a mean-field picture where $|q| \propto D/J$, the pressure-driven increase of T_c indicates a concomitant increase of J. At the same time, the pressure-driven reduction of $|q|$ implies a pressure dependence of D that is weaker than that of J for the explored pressure range.

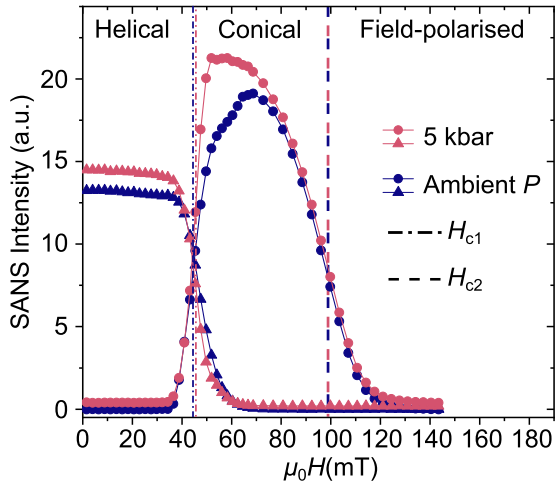

FIG. 4. Pressure and $\mu_0 H$ dependence at $T = 5$ K of the average SANS intensity due to the two helical domains described by $\mathbf{q}_1$ and $\mathbf{q}_2$ (triangles) and the single conical (circles) domain studied in the (001) scattering plane. The dash-dotted lines indicate the first critical field H_{c1}, which denotes the transition between helical and conical phases, while the dashed lines indicate the second critical field H_{c2} between the conical and field-polarized states.

Figure 4 shows the $\mu_0 H$ dependence at 5 K of the SANS intensity due to helical and conical order measured in the $\mu_0 H \perp \mathbf{k}_i$ geometry. From peaks that are found in the first magnetic field derivatives of the SANS intensity, we determined the pressure dependence of the critical magnetic field H_{c1} (dash-dotted lines on the graph), which separates the zero-field helical phase and the conical phase, and the critical magnetic field H_{c2} (dashed lines on the graph), which separates the conical phase from a field-polarized phase. Clearly, the pressure dependence of both critical fields is very weak. We determine H_{c2} at both ambient pressure and 5 kbar to be unchanged within uncertainty, namely, 99.5(5) and 99.1(5) mT, respectively. Our analysis shows that the critical field H_{c1} increases slightly by 2.5(1.0)% under pressure since $H_{c1}(P = 0\ \text{kbar}) = 44.6(3)$ mT and $H_{c1}(P = 5\ \text{kbar}) = 45.7(3)$ mT.

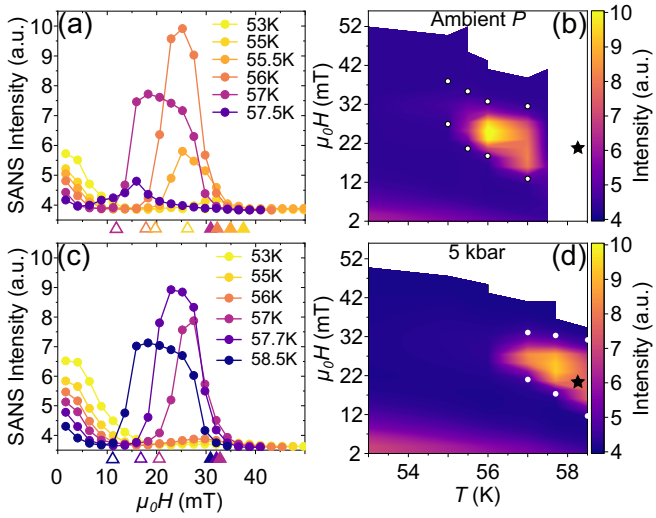

FIG. 5. (a) and (c) show the $\mu_0 H$ and T dependences of the SANS intensity at ambient pressure and $P = 5$ kbar, respectively. The open (solid) triangles indicate the lower (upper) transition fields of the skyrmion pocket. The color of the triangle depends on T. The finite intensity at the very lowest fields is due to the helical phase. (b) and (d) show color maps created from the scans shown in (a) and (c), which focus on the high-T portion of the $\mu_0 H$ and T phase diagrams at ambient pressure and $P = 5$ kbar, respectively. The white circles indicate SkL phase boundaries. The black star denotes the $\mu_0 H$ and T condition under which the data in Fig. 7 were collected.

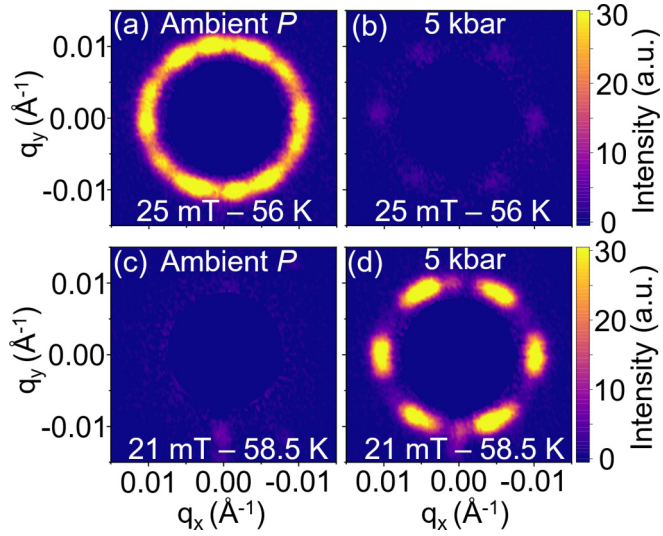

FIG. 6. Pressure stability of the SkL phase in Cu_2OSeO_3 in the $\mu_0 H \parallel \mathbf{k}_i$ geometry. SANS scattering patterns of the SkL at $T = 56$ K, $\mu_0 H = 25$ mT, and (a) ambient pressure or (b) $P = 5$ kbar. (c) and (d) show SANS patterns obtained at ambient pressure and $P = 5$ kbar, respectively, each with fixed $T = 58.5$ K, $\mu_0 H = 21$ mT. The panels are shown with a fixed intensity scale to emphasize differences in scattered SANS intensity for the different pressure conditions.

C. Pressure dependence of skyrmion phase stability

In Fig. 5 we summarize our measurements that demonstrate the easy quasihydrostatic pressure control of the parametric extent of the SkL phase. Figures 5(a) and 5(c) show the $\mu_0 H$ and T dependences of the SANS SkL intensities from which the upper- and lower-field SkL phase boundaries were determined. The determined phase boundaries are shown by white circles in the color map plots of the SANS intensity shown in Figs. 5(b) and 5(d). At ambient pressure, the largest T extent of the SkL phase is $T_c(P = 0) - 2.5(5)$ K, which is consistent with phase diagrams published elsewhere (see, for example, Refs. [2,13,44]). Under pressure, the maximum T extent of the SkL phase increases slightly to $T_c(P = 5\ \text{kbar}) - 3.0(5)$ K, with no otherwise significant change in the skyrmion pocket.

From the phase diagrams shown in Fig. 5, it is clear that for fixed T and $\mu_0 H$, the SkL stability can be tuned exclusively using applied pressure. We show this explicitly with SANS data presented in Fig. 6. Figures 6(a) and 6(b) show SkL SANS patterns at ambient pressure and $P = 5$ kbar, respectively, each at fixed $T = 56$ K and $\mu_0 H = 25$ mT. Under this particular T and $\mu_0 H$ condition, the SkL becomes less stable under pressure with respect to the competing conical phase,

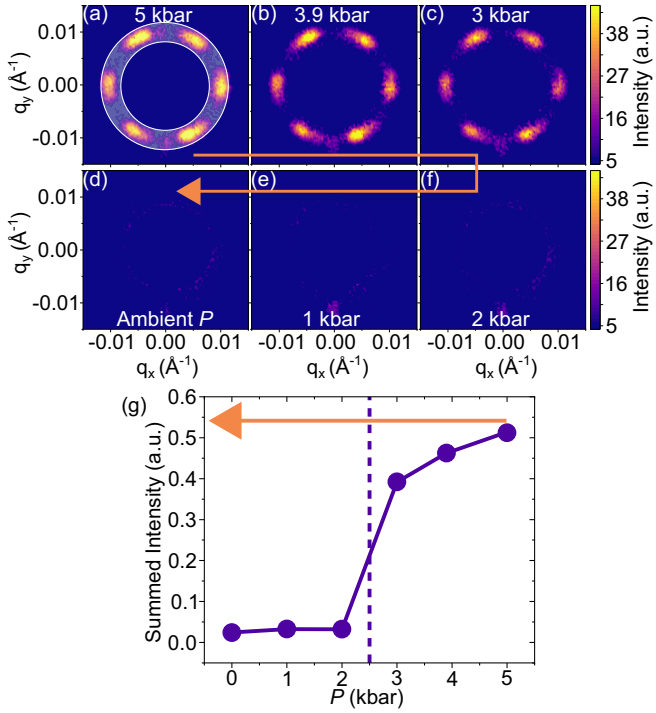

FIG. 7. (a) to (f) show the pressure-decreasing dependence of the SANS patterns obtained at fixed $T = 58.25(10)$ K and $\mu_0 H = 21$ mT. The shaded, annular area in (a) indicates the area of the detector over which the scattered intensity has been integrated for the graph in (g). (a) to (f) are presented with a fixed intensity scale. The orange arrows across all panels indicate the direction of pressure variation in the measurement.

as the SkL SANS intensity observed at ambient pressure becomes greatly suppressed. In contrast to pressure-driven destabilization, Figs. 6(c) and 6(d) show that at the fixed $T = 58.5$ K and $\mu_0 H = 21$ mT, the SkL phase stability is enhanced under $P = 5$ kbar compared with that at ambient pressure. In this particular case, the sample is below T_c in $P = 5$ kbar but in the paramagnetic state at ambient pressure.

Figure 6(a) also shows that a multidomain SkL is observed at $T = 56$ K and $\mu_0 H = 25$ mT, which is in the heart of the SkL pocket at ambient pressure. On the other hand, Fig. 6(b) shows that under $P = 5$ kbar, a weaker-intensity, single-domain SkL pattern is observed. While conceivable that the modified distribution of internal strains under pressure affects the SkL domain states, previous studies on Cu_2OSeO_3 at ambient pressure revealed the properties of SkL domain states to display a seemingly delicate dependence on temperature, magnetic field, and other effects such as thermal history [45,46,48,51,52]. Therefore, since the internal strain distributions in the sample are unknown at both ambient pressure and $P = 5$ kbar, the data at hand do not allow us to make conclusions about magnetostructural coupling effects on the SkL domain states. A future challenge will be to obtain a fully holistic understanding of the interplay between SkL orientation and domain states, their dependence on thermodynamic parameters, and the coupling with the crystal lattice.

Finally, in Fig. 7 we show in detail a direct, *in situ* pressure-driven transition between pressure-stabilized SkL and ambient-pressure paramagnetic phases. Starting from a stable SkL phase at $T = 58.25(10)$ K and $\mu_0 H = 21$ mT at 5 kbar, SANS patterns were recorded at various pressures upon pressure release. A particular effort was made to release the He gas pressure sufficiently slowly to avoid sample T variation due to evaporative cooling. For the data shown in Fig. 7, no T variation larger than 10 mK was observed on the sample thermometer. As seen in Fig. 7(g), the total scattered intensity from the SkL starts to fall smoothly as pressure is released before disappearing abruptly at $P_c = 2.5(5)$ kbar in a first-order manner. These data imply the persistence of a first-order transition boundary at T_c for $\mu_0 H = 21$ mT and the modest pressures explored here. Attempts were also made to drive the phase transition upon pressure increase at constant T and $\mu_0 H$, but T stability was lost when attempting to slowly pressurize the sample at cryogenic Ts with He gas supplied from room T.

IV. DISCUSSION

To summarize our experiments, from our data we establish key aspects of the microscopic magnetism and the $\mu_0 H \parallel [0\bar{1}1]$ magnetic phase diagram in Cu_2OSeO_3 for both ambient pressure and high quasihydrostatic $P = 5$ kbar. Under the applied pressure we find that T_c changes by $+2.8(2)\%$, while at low T the magnitude of the helical propagation vector $|q|$ changes by $-0.5(2)\%$ and H_{c1} changes by $+2.5(1.0)\%$, with H_{c2} unchanged within uncertainty. These experimentally determined variations can be related to changes in effective model parameters by $T_c \propto J$, $|q| \propto D/J$, $H_{c1} \propto K$, and $H_{c2} \propto D^2/J$, according to mean-field theory [9,13]. Here K denotes magnetic anisotropy. While measurements of T_c and H_{c1} provide independent measures of J and K, respectively, D is tangled up in both $|q|$ and H_{c2}, which both further depend on J. Nonetheless, a consistent description of all the pressure-induced variations of the experimentally determined quantities is found if D changes with pressure by $+2.2(1)\%$ and thus increases less slowly with pressure than J. Overall, the effect of the applied pressure is minor and does not lead to a significant modification of the structure of the phase diagram or absolute parameter space occupied by the SkL phase. Our data indicate that the T extent of the SkL phase below T_c increases slightly under pressure. This small increase would be consistent with the deduced increase of K, which is a parameter that is known to control the T extent of the SkL phase stability at the mean-field level [13,14].

The observed changes of T_c, H_{c1}, and H_{c2} induced by $P = 5$ kbar can be compared with results available from other reported quasihydrostatic pressure studies on Cu_2OSeO_3. From high-pressure ac susceptibility data at 6 kbar, Levatić *et al.* [13] reported a change in T_c of $+2.5\%$, which is comparable with that found in the present study. In contrast, however, are the reported changes in H_{c1} of $+15\%$ and in H_{c2} of -9% in the low-T limit. At the same time a large increase in T extent of the SkL phase to $\sim T_c - 10$ K is also reported, compared with $\sim T_c - 2$ K at ambient pressure. Qualitatively similar, although less pronounced, changes are also reported in the quasihydrostatic pressure study of Wu *et al.* [39]. In that work, the largest T extent of the SkL phase increases from $T_c - 3$ K at ambient pressure to $T_c - 5.2$ K at 5.22 kbar. These pressure-driven increases in SkL phase stability are not corroborated by the results in present study.

Instead, strong low-pressure dependences of the critical fields and the T extent of the SkL phase are more consistent with the response of chiral magnets under directional stress. In MnSi, detailed studies of single-crystal samples under compressive uniaxial stress reveal a strong correlation between the mutual directions of stress σ and $\mu_0 H$; a significant enhancement of skyrmion phase stability is observed for $\sigma \perp \mu_0 H$, while phase stability is suppressed for $\sigma \parallel \mu_0 H$ [32,33]. In both cases, T_c is suppressed slightly, while H_{c1} either increases or decreases strongly depending on the mutual directions of σ and $\mu_0 H$. Under quasihydrostatic pressure, $T_c \to 0$ at a well-known critical point near 14.6 kbar [25,53].

For Cu_2OSeO_3, with compressive stress $\sigma \parallel [110]$ and $\mu_0 H \parallel [1\bar{1}0]$, the study of Nakajima *et al.* [41] revealed the largest T extent of the SkL phase to almost double from $T_c - 1.6$ K at ambient pressure to $T_c - 2.7$ K for $\sigma \sim 1.01$ kbar. At the same time H_{c1} triples in the high-T range compared with that at ambient pressure. Taken together, the qualitative similarity between uniaxial pressure effects on the size of the SkL pocket and critical fields [32,33,41] and similar effects reported under quasihydrostatic high pressure in bulk measurements [13,39] implies that the latter data are affected by inadvertent directional pressure components. We postulate such pressure components can arise at low T in Refs. [13,39] due to the use of Daphne Oil 7373 as the PTM in both studies. Even if, in each study, the pressure changes themselves were performed at room T, where Daphne Oil 7373 remains liquid and within its hydrostatic limit, this PTM nonetheless freezes far above T_c at a T that varies linearly from ~182 K at ambient P to ~290 K at 1.9 GPa [54]. Therefore, nonhydrostatic pressure components can be induced due to the different relative contractions of the frozen PTM, sample, and pressure cell material upon cooling from the PTM freezing temperature to the measurement temperature. It becomes clear then that in general, it is challenging to eradicate entirely nonhydrostatic components of the P. Even in the present study performed under superior hydrostatic pressure conditions where the PTM freezes below T_c only when pressurized, directional strains in the sample are still not entirely suppressed, as evidenced by unequal populations of helical domains on ZFC. The influence of such strains on our main conclusions is considered to be unimportant, however, since no directional effects on the microscopic magnetism *within* helical domains is observed, and a generally modest pressure dependence of the entire magnetic phase diagram is observed up to $P = 5$ kbar.

V. SUMMARY

In summary, our small-angle neutron scattering study of the helimagnetic and skyrmion lattice phase diagram of Cu_2OSeO_3 showed only modest modification under quasihydrostatic He gas pressure up to 5 kbar. At a fixed temperature and magnetic field of 58.25(10) K and $\mu_0 H \parallel [1\bar{1}0] = 21$ mT, an *in situ* first-order pressure-driven transition between SkL and paramagnetic phases was demonstrated, indicating pressure as a third thermodynamic variable of the phase diagram of Cu_2OSeO_3 that can be considered for exploitation in order to achieve skyrmions at higher Ts in this archetypal insulating skyrmion host material.

While the reported quasihydrostatic pressure effects on Cu_2OSeO_3 are relatively minor, they nonetheless contrast strongly with more pronounced quasihydrostatic pressure effects on both the critical fields and thermal extent of the SkL pocket reported previously [13,39]. Since the previously reported pressure-dependent effects bear a strong qualitative resemblance to those observed from uniaxial pressure studies [32,33,41], we propose that the previous quasihydrostatic pressure studies of Cu_2OSeO_3 [13,39] are likely affected by directional stress components of the applied pressure. The origin of such directional stresses in these studies could be due to the use of a liquid PTM which, when freezing below room T but still far above T_c, can exert larger shear forces on a sample when cooled to the measurement T compared with the case when using compressed He gas [42]. Indeed, the high sensitivity of chiral magnetism to deviations from quasihydrostatic pressure conditions is well noted for samples immersed in a liquid PTM and pressurized using a typical clamp cell [27,42], and under such conditions it can be extremely challenging to suppress the influence of directional stress entirely. Thus, in general, claims of hydrostatic pressure-induced modifications of the topological magnetic properties and phase diagram must be considered very carefully if the sample is pressurized using a standard liquid PTM. This is particularly the case when there are no supporting data obtained by a microscopic probe such as neutron or resonant x-ray scattering which can provide direct indications for the existence of directional strain effects on the magnetism inside the sample [55].

Consequently, the quasihydrostatic high-pressure results for Cu_2OSeO_3 obtained here should be considered to be those obtained under the most hydrostatic pressure conditions to date on this material and thus provide a basis for comparison with future first-principles calculations of isotropically compressed Cu_2OSeO_3 [11]. On the experimental side, recent technical advances in a high-gas-pressure apparatus for neutron scattering will allow exploration of chiral magnets under gas pressure significantly higher than 5 kbar in the near future. This will provide a wider parameter space against which high-pressure observations may be compared with first-principle calculations.

The neutron scattering data that support the findings of this study are available from Institut Laue-Langevin [56].

ACKNOWLEDGMENTS

We thank S. Klotz and A. J. Kruchkov for helpful discussions and C. Payre for technical support with the gas pressure cell. This work was financially supported by the UK Skyrmion Project EPSRC Programme, Grant No. EP/N032128/1. Financial support from the Swiss National Science Foundation (SNSF) via the Sinergia network "NanoSkyrmionics" (Grant No. CRSII5_171003) and SNSF Project Grants No. 200021_153451 and No. 200021_188707 is gratefully acknowledged. The neutron scattering experiments were performed at the Institute Laue Langevin (ILL), Grenoble, France. The open access fee was covered by FILL2030, a European Union project within the European Commission's Horizon 2020 Research and Innovation programme under Grant Agreement No. 731096.

M.C. and N.R. contributed equally to this work.

[1] S. Mühlbauer, B. Binz, F. Jonietz, C. Pfleiderer, A. Rosch, A. Neubauer, R. Georgii, and P. Böni, Science **323**, 915 (2009).

[2] S. Seki, X. Z. Yu, S. Ishiwata, and Y. Tokura, Science **336**, 198 (2012).

[3] W. Münzer, A. Neubauer, T. Adams, S. Mühlbauer, C. Franz, F. Jonietz, R. Georgii, P. Böni, B. Pedersen, M. Schmidt, A. Rosch, and C. Pfleiderer, Phys. Rev. B **81**, 041203(R) (2010).

[4] H. Wilhelm, M. Baenitz, M. Schmidt, U. K. Rößler, A. A. Leonov, and A. N. Bogdanov, Phys. Rev. Lett. **107**, 127203 (2011).

[5] N. Nagaosa and Y. Tokura, Nat. Nanotechnol. **8**, 899 (2013).

[6] Y. Tokunaga, X. Z. Yu, J. S. White, H. Rønnow, D. Morikawa, Y. Taguchi, and Y. Tokura, Nat. Commun. **6**, 7638 (2015).

[7] K. Karube, J. S. White, N. Reynolds, J. L. Gavilano, H. Oike, A. Kikkawa, F. Kagawa, Y. Tokunaga, H. M. Rønnow, Y. Tokura, and Y. Taguchi, Nat. Mater. **15**, 1237 (2016).

[8] K. Karube, J. S. White, D. Morikawa, M. Bartkowiak, A. Kikkawa, Y. Tokunaga, T. Arima, H. M. Rønnow, Y. Tokura, and Y. Taguchi, Phys. Rev. Mater. **1**, 074405 (2017).

[9] J. Bak and M. H. Jensen, J. Phys. C **13**, L881 (1980).

[10] S. V. Maleyev, Phys. Rev. B **73**, 174402 (2006).

[11] O. Janson, I. Rousochatzakis, A. A. Tsirlin, M. Belesi, A. A. Leonov, U. K. Rößler, J. van den Brink, and H. Rosner, Nat. Commun. **5**, 5376 (2014).

[12] S. V. Grigoriev, A. S. Sukhanov, and S. V. Maleyev, Phys. Rev. B **91**, 224429 (2015).

[13] I. Levatić, P. Popčević, V. Šurija, A. Kruchkov, H. Berger, A. Magrez, J. S. White, H. M. Rønnow, and I. Živković, Sci. Rep. **6**, 21347 (2016).

[14] A. J. Kruchkov, J. S. White, M. Bartkowiak, I. Živković, A. Magrez, and H. M. Rønnow, Sci. Rep. **8**, 10466 (2018).

[15] X. Z. Yu, N. Kanazawa, Y. Onose, K. Kimoto, W. Z. Zhang, Y. Matsui, and Y. Tokura, Nat. Mater. **10**, 106 (2011).

[16] P. Milde, D. Köhler, J. Seidel, L. M. Eng, A. Bauer, A. Chacon, J. Kindervater, S. Mühlbauer, C. Pfleiderer, S. Buhrandt, C. Schütte, and A. Rosch, Science **340**, 1076 (2013).

[17] A. Bauer, M. Garst, and C. Pfleiderer, Phys. Rev. B **93**, 235144 (2016).

[18] Y. Okamura, F. Kagawa, S. Seki, and Y. Tokura, Nat. Commun. **7**, 12669 (2016).

[19] H. Oike, A. Kikkawa, N. Kanazawa, Y. Taguchi, M. Kawasaki, Y. Tokura, and F. Kagawa, Nat. Phys. **12**, 62 (2016).

[20] M. T. Birch, R. Takagi, S. Seki, M. N. Wilson, F. Kagawa, A. Štefančič, G. Balakrishnan, R. Fan, P. Steadman, C. J. Ottley, M. Crisanti, R. Cubitt, T. Lancaster, Y. Tokura, and P. D. Hatton, Phys. Rev. B **100**, 014425 (2019).

[21] J. S. White, I. Živković, A. J. Kruchkov, M. Bartkowiak, A. Magrez, and H. M. Rønnow, Phys. Rev. Appl. **10**, 014021 (2018).

[22] M. N. Wilson, M. Crisanti, C. Barker, A. Štefančič, J. S. White, M. T. Birch, G. Balakrishnan, R. Cubitt, and P. D. Hatton, Phys. Rev. B **99**, 174421 (2019).

[23] A. Štefančič, S. H. Moody, T. J. Hicken, T. M. Birch, G. Balakrishnan, S. A. Barnett, M. Crisanti, J. S. O. Evans, S. J. R. Holt, K. J. A. Franke, P. D. Hatton, B. M. Huddart, M. R. Lees, F. L. Pratt, C. C. Tang, M. N. Wilson, F. Xiao, and T. Lancaster, Phys. Rev. Mater. **2**, 111402(R) (2018).

[24] A. S. Sukhanov, P. Vir, A. S. Cameron, H. C. Wu, N. Martin, S. Mühlbauer, A. Heinemann, H. D. Yang, C. Felser, and D. S. Inosov, Phys. Rev. B **100**, 184408 (2019).

[25] C. Pfleiderer, G. J. McMullan, S. R. Julian, and G. G. Lonzarich, Phys. Rev. B **55**, 8330 (1997).

[26] C. Pfleiderer, S. R. Julian, and G. G. Lonzarich, Nature (London) **414**, 427 (2001).

[27] B. Fåk, R. A. Sadykov, J. Flouquet, and G. Lapertot, J. Phys.: Condens. Matter **17**, 1635 (2005).

[28] P. Pedrazzini, H. Wilhelm, D. Jaccard, T. Jarlborg, M. Schmidt, M. Hanfland, L. Akselrud, H. Q. Yuan, U. Schwarz, Y. Grin, and F. Steglich, Phys. Rev. Lett. **98**, 047204 (2007).

[29] M. Deutsch, P. Bonville, A. V. Tsvyashchenko, L. N. Fomicheva, F. Porcher, F. Damay, S. Petit, and I. Mirebeau, Phys. Rev. B **90**, 144401 (2014).

[30] M. Deutsch, O. L. Makarova, T. C. Hansen, M. T. Fernandez-Diaz, V. A. Sidorov, A. V. Tsvyashchenko, L. N. Fomicheva, F. Porcher, S. Petit, K. Koepernik, U. K. Rößler, and I. Mirebeau, Phys. Rev. B **89**, 180407(R) (2014).

[31] V. A. Sidorov, A. E. Petrova, P. S. Berdonosov, V. A. Dolgikh, and S. M. Stishov, Phys. Rev. B **89**, 100403(R) (2014).

[32] A. Chacon, A. Bauer, T. Adams, F. Rucker, G. Brandl, R. Georgii, M. Garst, and C. Pfleiderer, Phys. Rev. Lett. **115**, 267202 (2015).

[33] Y. Nii, T. Nakajima, A. Kikkawa, Y. Yamasaki, K. Ohishi, J. Suzuki, Y. Taguchi, T. Arima, Y. Tokura, and Y. Iwasa, Nat. Commun. **6**, 8539 (2015).

[34] N. Martin, M. Deutsch, J.-P. Itié, J.-P. Rueff, U. K. Rössler, K. Koepernik, L. N. Fomicheva, A. V. Tsvyashchenko, and I. Mirebeau, Phys. Rev. B **93**, 214404 (2016).

[35] D. M. Fobes, Y.-K. Luo, N. León-Brito, E. D. Bauer, V. R. Fanelli, M. A. Taylor, L. M. DeBeer-Schmitt, and M. Janoschek, Appl. Phys. Lett. **110**, 192409 (2017).

[36] V. A. Sidorov, A. E. Petrova, N. M. Chtchelkatchev, M. V. Magnitskaya, L. N. Fomicheva, D. A. Salamatin, A. V. Nikolaev, I. P. Zibrov, F. Wilhelm, A. Rogalev, and A. V. Tsvyashchenko, Phys. Rev. B **98**, 125121 (2018).

[37] L. J. Bannenberg, R. Sadykov, R. M. Dalgliesh, C. Goodway, D. L. Schlagel, T. A. Lograsso, P. Falus, E. Lelièvre-Berna, A. O. Leonov, and C. Pappas, Phys. Rev. B **100**, 054447 (2019).

[38] C. L. Huang, K. F. Tseng, C. C. Chou, S. Mukherjee, J. L. Her, Y. H. Matsuda, K. Kindo, H. Berger, and H. D. Yang, Phys. Rev. B **83**, 052402 (2011).

[39] H. C. Wu, T. Y. Wei, K. D. Chandrasekhar, T. Y. Chen, H. Berger, and H. D. Yang, Sci. Rep. **5**, 13579 (2015).

[40] S. Seki, Y. Okamura, K. Shibata, R. Takagi, N. D. Khanh, F. Kagawa, T. Arima, and Y. Tokura, Phys. Rev. B **96**, 220404(R) (2017).

[41] T. Nakajima, V. Ukleev, K. Ohishi, H. Oike, F. Kagawa, S. Seki, K. Kakurai, Y. Tokura, and T. Arima, J. Phys. Soc. Jpn. **87**, 094709 (2018).

[42] S. Klotz, *Techniques in High Pressure Neutron Scattering* (CRC Press, Boca Raton, FL, 2012).

[43] S. Klotz, J.-C. Chervin, P. Munsch, and G. La Marchand, J. Phys. D **42**, 075413 (2009).

[44] T. Adams, A. Chacon, M. Wagner, A. Bauer, G. Brandl, B. Pedersen, H. Berger, P. Lemmens, and C. Pfleiderer, Phys. Rev. Lett. **108**, 237204 (2012).

[45] S. Seki, J.-H. Kim, D. S. Inosov, R. Georgii, B. Keimer, S. Ishiwata, and Y. Tokura, Phys. Rev. B **85**, 220406(R) (2012).

[46] J. S. White, I. Levatić, A. A. Omrani, N. Egetenmeyer, K. Prša, I. Živković, J. L. Gavilano, J. Kohlbrecher, M. Bartkowiak,

H. Berger, and H. M. Rønnow, J. Phys.: Condens. Matter **24**, 432201 (2012).

[47] J. S. White, K. Prša, P. Huang, A. A. Omrani, I. Živković, M. Bartkowiak, H. Berger, A. Magrez, J. L. Gavilano, G. Nagy, J. Zang, and H. M. Rønnow, Phys. Rev. Lett. **113**, 107203 (2014).

[48] K. Makino, J. D. Reim, D. Higashi, D. Okuyama, T. J. Sato, Y. Nambu, E. P. Gilbert, N. Booth, S. Seki, and Y. Tokura, Phys. Rev. B **95**, 134412 (2017).

[49] C. D. Dewhurst, Institut Laue-Langevin, Technical Report No. ILL03DE01T, 2003 (unpublished), https://www.ill.fr/lss/grasp.

[50] J.-P. Pinceaux, J.-P. Maury, and B. J.-M, J. Phys. Lett. **40**, 307 (1979).

[51] L. J. Bannenberg, F. Qian, R. M. Dalgliesh, N. Martin, G. Chaboussant, M. Schmidt, D. L. Schlagel, T. A. Lograsso, H. Wilhelm, and C. Pappas, Phys. Rev. B **96**, 184416 (2017).

[52] S. Pöllath, J. Wild, L. Heinen, T. N. G. Meier, M. Kronseder, L. Tutsch, A. Bauer, H. Berger, C. Pfleiderer, J. Zweck, A. Rosch, and C. H. Back, Phys. Rev. Lett. **118**, 207205 (2017).

[53] R. Ritz, M. Halder, C. Franz, A. Bauer, M. Wagner, R. Bamler, A. Rosch, and C. Pfleiderer, Phys. Rev. B **87**, 134424 (2013).

[54] M. S. Torikachvili, S. K. Kim, E. Colombier, S. L. Bud'ko, and P. C. Canfield, Rev. Sci. Instrum. **86**, 123904 (2015).

[55] L. Deng, H.-C. Wu, A. P. Litvinchuk, N. F. Q. Yuan, J.-J. Lee, R. Dahal, H. Berger, H.-D. Yang, and C.-W. Chu, Proc. Natl. Acad. Sci. USA **117**, 8783 (2020).

[56] https://doi.ill.fr/10.5291/ILL-DATA.5-42-414.